

Research Article

Hierarchical N- and O-Doped Porous Carbon Composites for High-Performance Supercapacitors

Ben-Xue Zou ^{1,2}, Yan Wang,¹ Xiaodong Huang,¹ and Yanhua Lu ²

¹Department of Chemical Engineering, Eastern Liaoning University, Dandong 118001, China

²Liaoning Key Laboratory of Functional Textile Materials, Dandong 118001, China

Correspondence should be addressed to Ben-Xue Zou; benxue_dd@163.com and Yanhua Lu; yanhualu@aliyun.com

Received 26 December 2017; Revised 27 February 2018; Accepted 27 March 2018; Published 27 June 2018

Academic Editor: Suresh Kannan Balasingam

Copyright © 2018 Ben-Xue Zou et al. This is an open access article distributed under the Creative Commons Attribution License, which permits unrestricted use, distribution, and reproduction in any medium, provided the original work is properly cited.

Hierarchical N- and O-doped porous carbon composites were prepared by hydrothermally assembling of silk fibers with low molecular weight phenolic resin, followed by carbonization and KOH activation process. Silk fibroin is expected to provide nitrogen and oxygen functionalities for the final composite carbon. The introduction of thin layer graphitic structures of low molecular weight phenolic resin-derived carbon offers more abundant structures, low resistance, and hierarchical porosity with a high BET surface area of $1927 \text{ m}^2 \cdot \text{g}^{-1}$. The composition and electrochemical properties of the composite carbon have been studied as a function of the annealing temperature for KOH activation process. The obtained carbon composite exhibits high specific capacitance as high as $330 \text{ F} \cdot \text{g}^{-1}$ ($1000 \text{ mF} \cdot \text{cm}^{-2}$) at $0.5 \text{ A} \cdot \text{g}^{-1}$, good rate capability, and excellent cycling stability (91% of capacitance retention after 10000 cycles) in 6 M KOH electrolyte.

1. Introduction

Electrochemical capacitors (ECs), also called supercapacitors or ultracapacitors, are considered to be promising devices for high power demand and long cycle life [1–4]. ECs can harvest and release more energy within time less than 10 s and can be used for an almost unlimited number of charge and discharge cycles, which are superior to or distinctive from Li-ion batteries. Thus, ECs are playing important role in the energy storage devices requiring fast burst of energy and back-up of power sources.

Carbon materials have been widely employed as electrodes for ECs because of their fast charge/discharge kinetics, bipolar operational flexibility, and good stability and because of being environmentally friendly [5–8]. It has been demonstrated that the initial material has a significant impact on the formation mechanism, the specific surface area, and the composition of the final carbon materials [9–12]. The different pore size distribution can be obtained by different physical and chemical activation methods using KOH, CO_2 , or steam as activating agent [13–16]. Kim et al. found that the steam-activated silk carbons have smaller capacitance in gravimetric

unit than that of the KOH-activated silk carbon (with nearly doubled gravimetric capacitance), but the steam-activated silk carbons showed comparable volumetric capacitance to that of the conventional phenolic resin-based carbon prepared by KOH activation [17]. Thus, they suggested that the steam-activated silk carbon was superior to the conventional KOH-activated phenolic resin carbon materials regarding to the production cost. Zhu et al. synthesized a porous carbon by using KOH chemical activation of exfoliated graphite oxide [18]. This carbon electrode exhibited a large surface area of up to $3100 \text{ m}^2 \cdot \text{g}^{-1}$ and a specific capacitance of $166 \text{ F} \cdot \text{g}^{-1}$ in BMIM BF_4/AN electrolyte.

Moreover, the modification with heteroatom is an important route to improve the electrochemical performance of carbon materials for ECs [19–22]. Heteroatom doping such as N and O is expected to enhance the surface polarity and the electron-donor affinity and thus improve the interfacial interaction between carbon electrode and electrolyte [23–26]. N and O functionalities can significantly enhance the wettability, hydrophilicity, and compatibility, which are beneficial for the electrolyte ions accessible to the micropores of carbon materials, thus leading to high

power output and rate performance of carbon electrode. They can also give rise to Faradic capacitance through electrochemical redox reactions. N and O functional groups are usually introduced into carbon materials by employing nitrogen- and oxygen-containing compounds as a nitrogen and oxygen dopant. It is generally accepted that using nitrogen-containing polymers such as polyimide, melamine, polyvinylpyridine, polypyrrole, and cyanamide as a nitrogen dopant by direct carbonization process is a simple and controllable method. Lin et al. have recently reported N-doped ordered mesoporous few layer carbons with extraordinary capacitance of $855 \text{ F}\cdot\text{g}^{-1}$ in aqueous electrolytes for electrochemical energy storage [27]. Wang et al. used urea-modified lignin as raw materials to produce N-doped porous carbon with high specific capacitance and low resistance for electric double-layer capacitors (EDLCs) [28]. Chen et al. explored N-doped graphene by carbonization process of aromatic polyimide films deposited on the surface of graphene by molecular layer deposition [29]. This N-doped graphene exhibited a high specific capacitance of $290 \text{ F}\cdot\text{g}^{-1}$ at a current density of $1 \text{ A}\cdot\text{g}^{-1}$ in 6 M KOH electrolyte. Recently, N- and O-codoped carbon materials have been explored for ECs which is expected to produce the synergistic effect and significantly enhance the capacitance performance [23, 30, 31].

In this work, high porosity of N- and O-doped carbon composites was successfully prepared by hydrothermal reaction, carbonization, and KOH activation process, with silk fibers and low molecular weight phenolic resin as carbon sources. The silk fiber networks were used as the matrix to incorporate the low molecular weight phenolic resin during the hydrothermal reaction. The introduction of low molecular weight phenolic resin provides more abundant structures, high conductivity, and hierarchical porosity for carbon composite materials. The further KOH activation process makes the carbon composite larger surface area and hierarchical opened pores. The resulting porous carbon possesses a high specific capacitance of $330 \text{ F}\cdot\text{g}^{-1}$ and excellent charge and discharge rates with high porosity and high specific surface area.

2. Experimental Section

2.1. Preparation of Hierarchical N- and O-Doped Porous Carbon Composites. The hierarchical N- and O-doped porous carbon composites were prepared with silk fibroin as starting materials. Firstly, the amount of silk tussah cocoon was immersed in 0.3 M NaOH solution for 24 h to obtain dispersive silk fibroin (SF), followed by washing with deionized water and drying at 80°C for 2 h. Then, the coating of low molecular weight phenolic resin on silk fibroin (SF/PR) was prepared by hydrothermal reaction similar to our previous report [32]. After that, the composite (SF/PR) was carbonized at 600°C for 2 h under pure nitrogen atmosphere at a heating rate of $10^\circ\text{C}/\text{min}$. The N_2 flow rate was adjusted 5–10 ml/min. The as-made carbon composite was ground to fine powders and mechanically mixed with 4-fold amount of KOH (weight ratio, KOH/carbon) for chemical activation. The chemical activation process was carried out under a N_2 atmosphere with tubular furnace individually at 700°C , 800°C , and 900°C to obtain samples KCP-700, KCP-800,

and KCP-900 for 2 h, respectively. Finally, the obtained carbon samples were placed in 20 ml 0.1 M HCl, stirred for 0.5 h, and washed with deionized water until the pH stabilized at 7.0. To illustrate the advantage of the carbon composite KCP, pure silk fibroin-derived carbon (named as KSW) without coating of phenolic resin was also prepared.

2.2. Material Characterization. The morphologies of the samples were observed with field emission scanning electron microscopy (FESEM, Carl Zeiss, Germany) and transmission electron microscopy (TEM, JEM2010-HR, 200 kV). Thermogravimetric analysis (TGA, NETZSCH STA 449 F3, Germany) was carried out from room temperature to 1000°C at the heating rate of $30^\circ\text{C}/\text{min}$ under inert atmosphere with Ar. Raman spectra were performed using confocal laser micro Raman spectrometer (HR800UV, HORIBA Jobin Yvon, France) with the excitation wavelength at 633 nm. XPS spectra were recorded on Thermo ESCALAB 250 electron spectrometer using Al $K\alpha$ radiation (1486.6 eV). The porous structure of the carbon was evaluated by the classical analysis of nitrogen adsorption-desorption isotherms using ASAP 2020 instrument at -196°C . The pore-size distributions were calculated via the Dubinin-Astakhov and BJH (Barrett-Joyner-Halenda) methods. The specific surface areas were calculated using Brunauer-Emmett-Teller (BET) equation. The pore volume was obtained from the adsorbed amount at a relative pressure of $P/P_0 = 0.97$.

2.3. Electrochemical Measurements. Electrochemical experiments were carried out on a CHI660E potentiostat in a three-electrode cell with a platinum plate as the counter electrode and saturated calomel electrode (SCE) as the reference electrode. Carbon cloth was used as the working electrode's current collector. The electrode active materials (including the pure KSW, composites KCP-700, KCP-800, and KCP-900) were firstly separately mixed with carbon colloid at a weight ratio of 3:1 in ethanol. The obtained pastes were then separately coated onto carbon cloth with a working area of $1.5 \times 1.2 \text{ cm}^2$. The mass loading of the two electrodes was about 6 mg. Electrochemical capacitive performances of the electrodes were studied by cyclic voltammetry (CV), chronopotentiometry (CP), and electrochemical impedance spectroscopy (EIS) with 6 M KOH electrolyte. EIS spectra were scanned from a frequency range of 100 kHz to 10 MHz with the operating potential of 0 V and the potential amplitude of 5 mV. Symmetric ECs were assembled by using KCP fixed on carbon cloth as two electrodes in 6 M KOH electrolyte solution.

3. Results and Discussion

3.1. Characterization of KCP Carbon Composite. To determine the carbonization temperature for the initial hydrothermally assembled composite of silk fibers and low molecular phenolic resin (SF/PR), thermogravimetric analysis profiles of the composite SF/PR, as well as the pristine silk fibers (SF), are represented in Figure 1. The original decomposition temperature for SF/PR composite (ca. 320°C) is slightly higher than that of the pristine SF (ca. 294°C), indicating that

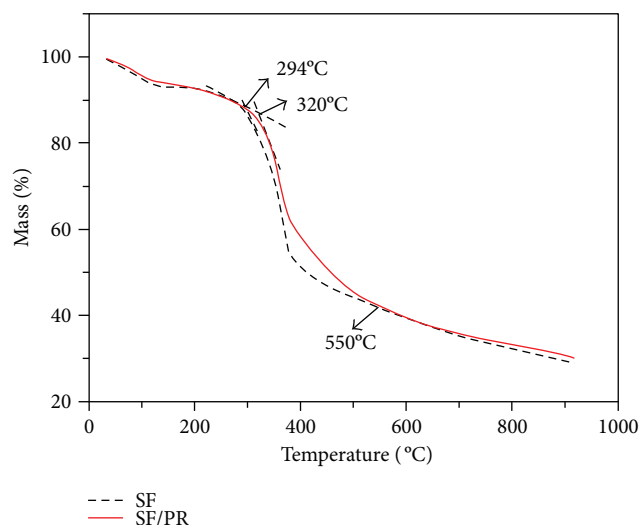


FIGURE 1: Thermogravimetric analysis profiles of pristine SF and SF/PR composite.

the thermal stability of SF/PR composite was enhanced by the introduction of phenolic resin. A drastic weight loss between 320 and 550°C is accompanied by the loss of hydrated water and the decomposition of nitrogen/oxygen functionalities [17]. The weight loss tends to be slow above 550°C, implying that the thermal treatment temperature of 600°C is high enough for the carbonization of the SF/PR composite.

The morphologies of the final KCP sample (derived from the composite SF/PR after carbonization and KOH activation) were examined by FESEM. The typical SEM image results show the final products KCP-800 and KCP-900 have abundant morphologies and microstructures. As shown in Figures 2(a) and 2(b), plenty of pores with different pore size were homogeneously distributed in the honeycomb-like or sponge-like bulk, ranging from micropores (<2 nm) to mesopores (e.g., 2~50 nm) to macropores (e.g., >50 nm). The opened pore size of KCP-800 is smaller than that of KCP-900 by comparing Figures 2(a) and 2(b), indicating the higher activation temperature leads to larger pores in the carbon samples. Figure 2(c) shows much feather duster-like or tree-like structures in the carbon product, which possess axis in the middle of the bulk and split layers with much opened narrow slit. SEM image of Figure 2(d) also presented lamellar structure with plenty of pores between layers. These lamellar platelet structures may be derived from low molecular weight phenolic resin raw materials, which are very different from the silk fiber structures. It should be pointed out that the tree-like or branched structures which are made of mesoporous channels with micropores around different branches have been reported to be possible ideal electrode because these mesopores should be channels for ions in the electrolyte to the abundant number of micropores throughout the electrode [5].

The SEM images clearly present varied microstructures with numerous hierarchical opened pores, which construct a three dimensional (3D) distribution of a porous material. These 3D networks of pores are originated from the thermal treatment process and followed KOH activation process.

During the first carbonization step, micro- and mesopores are generated in the carbon product due to small molecule of gases (CO_x , NO_x , H_2O , etc.) produced and released. The further KOH activation process yields a 3D network of nanoscale pores [30, 33]. The TEM images with a number of light dots presented as Figure 2(e) further corroborate dense pore structures with a distribution of pore sizes between ~1 nm and ~10 nm. And Figure 2(f) illustrates curved graphene-like sheets in the KCP-800 sample, which is desirable for a higher conductivity, higher surface area, and better capacitive performance.

The porous structure of KCP-800 was further confirmed by nitrogen adsorption and desorption measurements. The isotherm, as shown in Figure 3(a), reveals a steep increase of nitrogen adsorption in the initial part of low relative pressure ($P/P_0 < 0.1$), which is attributed to the accessible micropore filling, and the hysteresis loop in the relative high pressure region ($P/P_0 > 0.4$) which is associated with capillary condensation taking place in the mesopores. The isotherm reveals a combined I/IV type isotherm and limiting adsorption over a wide range of P/P_0 which is an indicative of H4 hysteresis loop according to the International Union of Pure and Applied Chemistry (IUPAC) classification [34]. Type H4 loop appears to be associated with narrow slit-like mesopores, and the type I isotherm character is an indicative of microporosity. The BET surface area and total pore volume reached about $1927 \text{ m}^2 \cdot \text{g}^{-1}$ and $0.83 \text{ cm}^3 \cdot \text{g}^{-1}$, respectively, which is expected to provide large contact area and space between the electrode and electrolyte. From the pore-size distribution curve shown in the inset of Figure 3(a), it is evident that the micro- and mesopores less than 5 nm are dominant in the KCP-800 sample. The adsorption average pore width by BET is 3.19 nm, which could be accessible electrochemically for electrolyte solution. The total pore volume is $\sim 0.83 \text{ cm}^3 \cdot \text{g}^{-1}$, ranging from the pore size of 1.7 to 300 nm, assuming the hierarchical nanopore structure of KCP-800 sample, which appears to be agreeable to the SEM and TEM results. This hierarchical pore structure with high surface area and pore volume is desirable for charge transfer in low resistance.

For comparison, Figure 3(b) shows the isotherm profiles of single-silk carbon KSW-800, together with its pore-size distribution curve. The low pressure hysteresis is observed extending to the lowest attainable pressures in KSW-800, which is distinct from that of the composite KCP-800. This phenomenon is thought to be associated with the swelling of a nonrigid porous structure or with the irreversible uptake of molecules in pores of about the same width as that of the adsorbate (N_2), implying that the introduction of low molecular weight phenolic resin into the silk fibers may change the mechanism of activation process and thus alter the porous structures of the carbon composite [34]. The pore-size distribution curves indicate the superiority of KCP-800 to single KSW-800 in terms of accumulated pore volume and hierarchical pore-size distribution.

Raman spectroscopy is performed to identify the structure of graphite- and graphene-based species. The Raman spectra (Figure 4(a)) clearly indicated the D band at 1335 cm^{-1} , the G band at 1591 cm^{-1} , and 2D at 2700 cm^{-1} . The D band at 1335 cm^{-1} is associated with disordered or functionality-

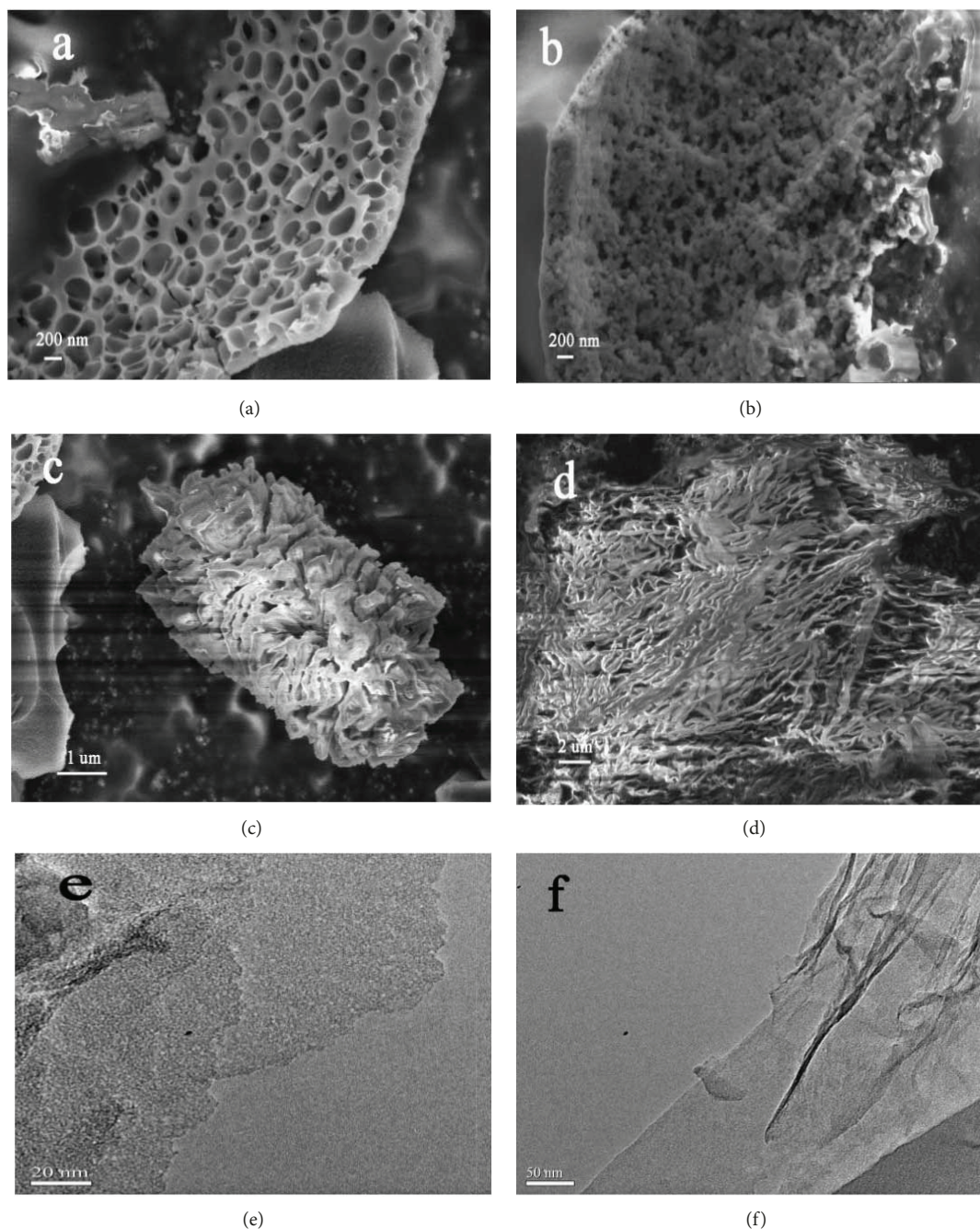


FIGURE 2: (a) Low resolution of SEM for KCP-900. (b–d) Low resolution of SEM for KCP-800. (e, f) High resolution of TEM for KCP-800.

enriched graphite [35]. The high G-band peak at 1591 cm^{-1} reflects the presence of graphite/graphene structures. The intensity ratio of I_G/I_D is about 1.0, suggesting that the disordered or functional group-doped graphite coexists with the ordinary graphitic materials [36].

The elemental composition and chemical states were investigated by means of XPS. The XPS survey spectrum shown in Figure 4(b) reveals signals of C, O, and N elements, indicating the presence of oxygen and nitrogen functionalities. XPS analysis results showed that the composition ratio of N/C is about 1.9% and that of O/C is about 16.0%. The involvement of nitrogen and oxygen can dramatically

improve the wettability, hydrophilicity, and compatibility for KCP-800 in the electrolyte solution. These natures, as well as the high porosity, may offer an appreciate reservoir for electrolyte ion transport which will increase the charge-transfer efficiency and create a large capacitance. The C1s spectrum (Figure 4(c)) was deconvoluted into four component peaks at binding energy ca. 284.7 eV for C-C, 284.8 eV for C=C, 285.9 eV for C-N, and 288.6 eV for C-O [36]. The N1s peak as shown in Figure 4(d) can be deconvoluted into two component peaks, namely, pyrrolic N (N-5, 399.9 eV) and quaternary N (N-Q, 400.9 eV) [37]. The presence of the N-Q bond can facilitate the electron transfer and cause

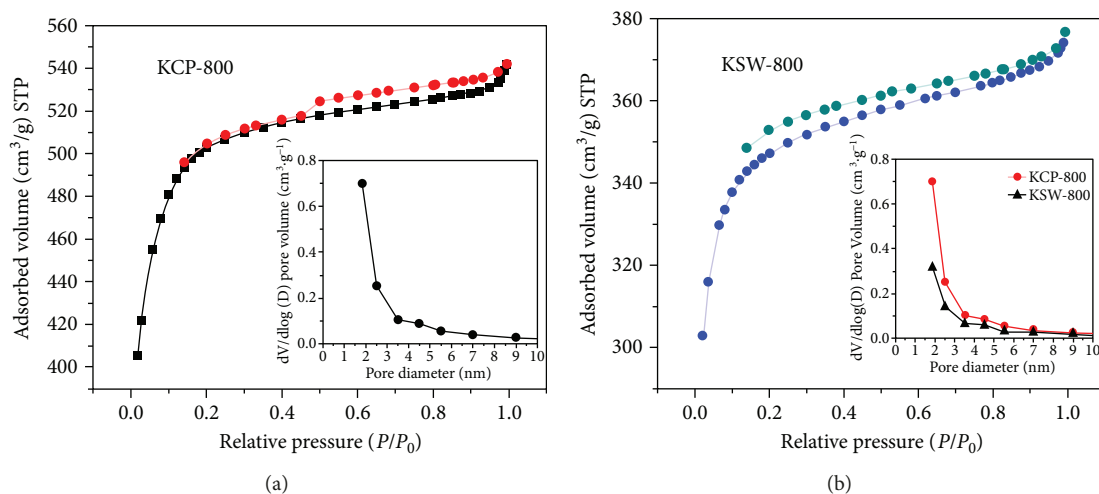


FIGURE 3: (a) N_2 adsorption-desorption isotherms of KCP-800 and pore-size distribution shown inset. (b) N_2 adsorption-desorption isotherms of KSW-800 and pore-size distribution shown inset.

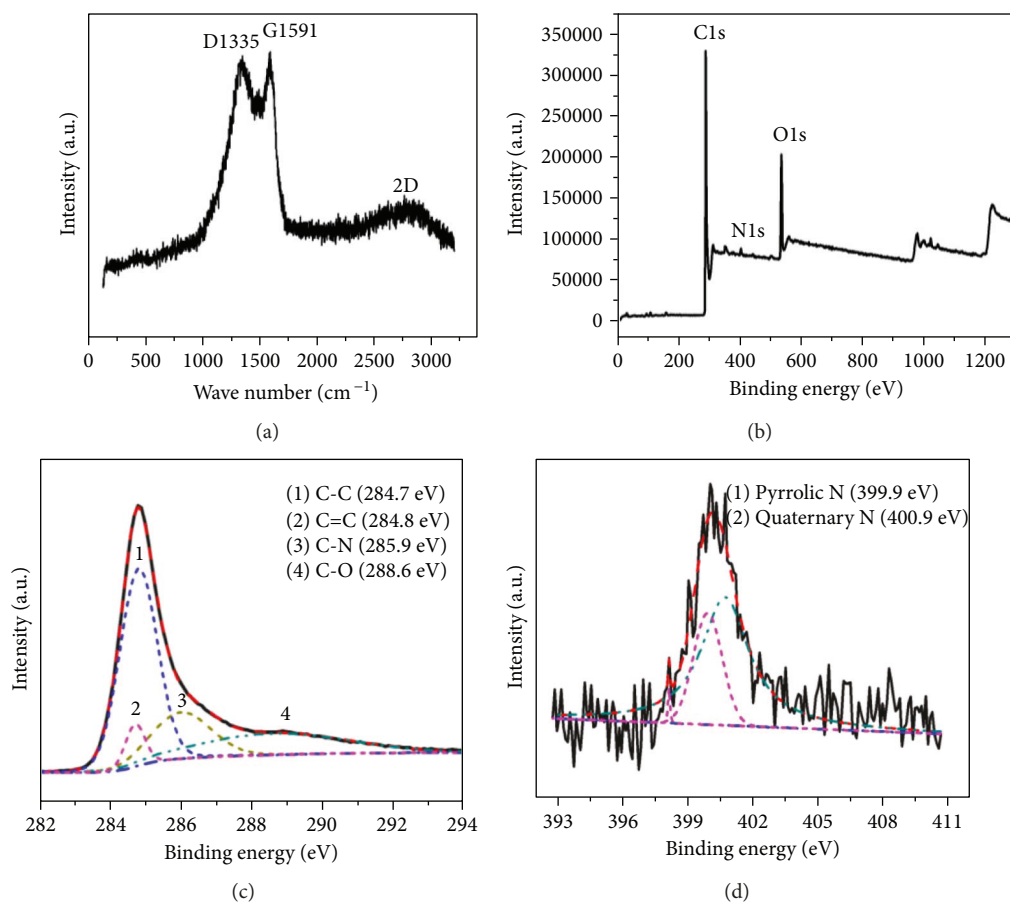


FIGURE 4: (a) Raman spectra of KCP-800. (b) XPS survey spectra of KCP-800. (c-d) High-resolution XPS spectra of deconvoluted C1s and N1s peaks.

the enhancement of the conductivity of carbon materials, which is beneficial for rate and cycling performance of supercapacitors. In addition, the presence of pyrrolic N is assumed to contribute the Faradaic reaction-based pseudocapacitive and thus increase the capacitance performance of the

electrode [38, 39]. The mechanism of redox reaction in acidic electrolyte (e.g., H_2SO_4) for N-doped carbon has been explained by the Lewis base behavior of the nitrogen functionalities on the carbon electrode. The possibilities of redox reactions for N-doped carbon in KOH electrolyte were also

TABLE 1: Porosity parameters and element composition by XPS of the carbon samples.

	Raw materials	Activity temperature (°C)	BET surface area (m ² /g)	Cumulative volume of pores (cm ³ /g)	N/C content (at.%)	O/C content (at.%)
KCP-700	Silk/LPR	700	911	0.043	3.44	35.9
KCP-800	Silk/LPR	800	1927	0.127	1.9	16.0
KCP-900	Silk/LPR	900	1886	0.160	2.1	16.2
KSW-800	Silk	800	1334	0.082	8.8	22.2

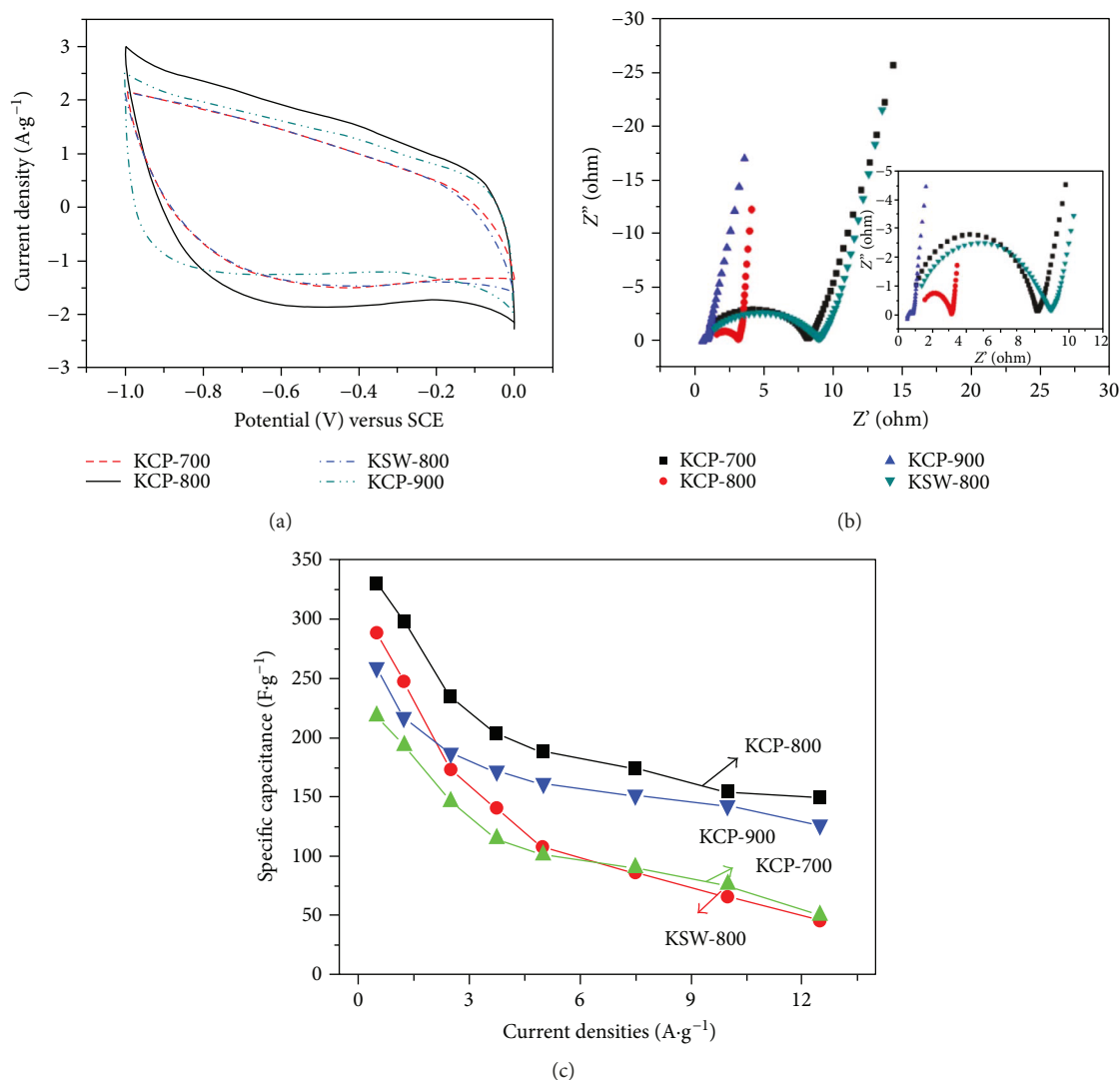


FIGURE 5: (a) CV curves of composites KCP-700, KCP-800, and KCP-900 electrodes and single-silk carbon KSW-800 electrode at 10 mV/s. (b) Nyquist plots for those electrodes measured at 0 V DC potential in the frequency range of 100 kHz to 10 MHz. (c) Specific capacitance of the four samples at different current densities in 6 M KOH electrolyte.

elucidated by previous reports [40]. It was assumed that the pyrrolic N (N-5) can be electrochemical oxidized to pyridone nitrogen (N-5 (OH)) in KOH electrolyte. The pyridone nitrogen atoms are considered as pyridine nitrogen atoms with one adjacent carbon atom that absorbs a hydroxyl group.

The porous structure and chemical composition of carbonaceous materials are summarized in Table 1. These

values are considered to be useful for understanding the relationships of many properties of the carbon materials. The BET surface area and cumulative pore volume of carbon composite KCP-800 are much higher than those of single-silk carbonaceous KSW-800, indicating that the introduction of low molecular weight phenolic resin provides more abundant structures and porosities for carbon composite

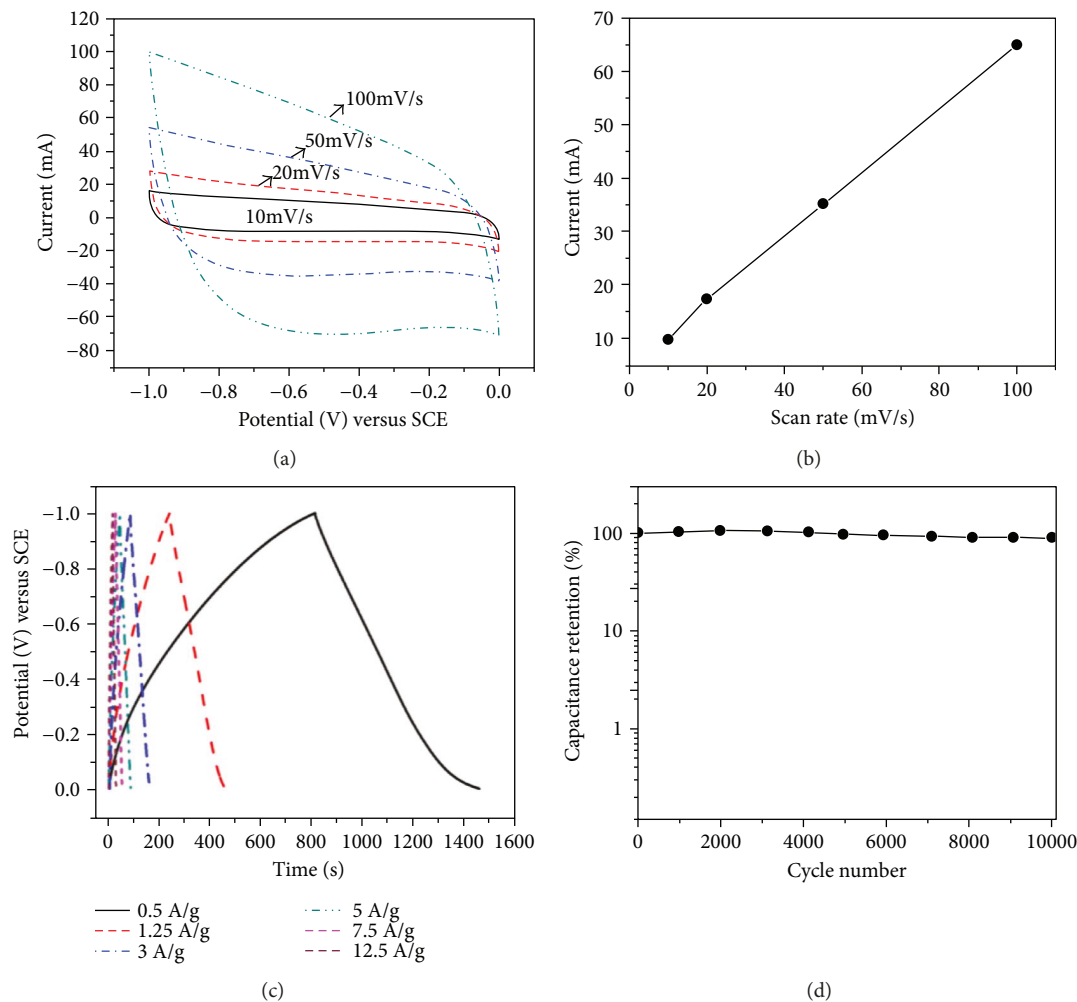


FIGURE 6: (a) CV curves of KCP-800 at various scan rates. (b) The dependence of the discharge current at -0.5 V on scan rate. (c) Galvanostatic charge/discharge profiles at various charge-discharge current densities from 0.5 to 12.5 $\text{A}\cdot\text{g}^{-1}$. (d) Capacitive retention of KCP-800 at a current density of 3 $\text{A}\cdot\text{g}^{-1}$ over 10000 cycles in 6 M KOH electrolyte.

TABLE 2: Comparison of the specific capacitance of carbon-based electrode in the literature.

Materials	Specific capacitance	Area capacitance	Reference
N-doped ordered mesoporous carbon	$227 \text{ F}\cdot\text{g}^{-1}$ ($0.2 \text{ A}\cdot\text{g}^{-1}$)		[12]
P-doped carbon	$133 \text{ F}\cdot\text{g}^{-1}$ ($10 \text{ A}\cdot\text{g}^{-1}$)	$146 \text{ mF}\cdot\text{cm}^{-2}$	[19]
N-doped graphene	$286 \text{ F}\cdot\text{g}^{-1}$ ($0.5 \text{ A}\cdot\text{g}^{-1}$)		[21]
N- and O-doped 3D porous carbon	$318 \text{ F}\cdot\text{g}^{-1}$ ($0.5 \text{ A}\cdot\text{g}^{-1}$)		[30]
N- and O-doped carbon	$302 \text{ F}\cdot\text{g}^{-1}$ ($5 \text{ A}\cdot\text{g}^{-1}$)		[31]
Porous carbon	$255 \text{ F}\cdot\text{g}^{-1}$ ($0.5 \text{ A}\cdot\text{g}^{-1}$)		[35]
N-doped graphene	$324 \text{ F}\cdot\text{g}^{-1}$ ($0.5 \text{ A}\cdot\text{g}^{-1}$)		[36]
CVT-on-VG	$278 \text{ F}\cdot\text{g}^{-1}$ (10 mV^{-1})	$36 \text{ mF}\cdot\text{cm}^{-2}$	[43]
Porous carbon	$296.2 \text{ F}\cdot\text{g}^{-1}$ ($0.05 \text{ A}\cdot\text{g}^{-1}$)		[44]
Porous N-doped carbon	$330 \text{ F}\cdot\text{g}^{-1}$ ($0.5 \text{ A}\cdot\text{g}^{-1}$)	$1000 \text{ mF}\cdot\text{cm}^{-2}$	This work

materials. Moreover, the activated carbon composite KCP-800 shows the highest BET surface area and moderate cumulative pore volume among the carbon samples. KCP-900 shows the highest cumulative volume of pores, indicating

that the higher activation temperature may promote the formation of more porous structures [16]. The relative amounts of oxygen (O) and nitrogen (N) on the surface are also shown in Table 1. The composition ratio of N/C of the composite

samples is about 3.55% after carbonization at 600°C. The N/C ratio is changed to 3.44%, 1.9%, and 2.2% after KOH activation at 700°C, 800°C, and 900°C, respectively. The O/C ratio shows similar trend with the increase of the activation temperature. The observable changes of the N/C and O/C ratios are taken place at temperatures above 700°C, implying further decomposition of nitrogen functionalities or digestion of the carbon by KOH during the activation process.

3.2. Capacitive Performance of Carbon Composite KCP Electrode. Cyclic voltammetric scans were conducted in 6 M KOH at a scan rate of 10 mV·s⁻¹ to investigate the electrochemical performance of the carbon composite KCP (Figure 5(a)). All these electrodes with the same mass loading (about 6 mg) display similar rectangular shapes in their CV curves and no significant gas evolution in the negative potential range of -1.0~0 V. These wide negative potential ranges can be ascribed to electrochemical reactions of N and O functionalities on these electrodes which lead to higher overpotentials for gas evolution and the increase of energy density for supercapacitors [41]. KCP-800 exhibits the highest current density among these electrodes, indicating the better pseudocapacitive behavior of KCP-800. Otherwise, from the CV curves, KCP-800 and KCP-900 show more rectangular shapes and faster current transfer respond at the potential limits, indicating that dealing with higher temperature in KOH activity process may provide more hierarchical porous structures for carbon materials and thus give rise to the lower resistance for charge transfer throughout the electrode.

The electrical characterization of capacitor electrodes is usefully evaluated with frequency response of their impedance. Figure 5(b) shows frequency responses in the range of 100 kHz to 10 MHz for these electrodes. The distorted semicircle in the high-frequency region and the nearly vertical linear in the low-frequency region indicate the typical capacitive behavior of these electrodes. The RC semicircle is associated with electrochemical process at the electrode-electrolyte interface, which is described as the capacitance (C) in parallel with the charge-transfer resistance (R_{ct}) due to the charge exchange of electroactive functionality groups such as C-N, C-OH, and -COOH at the interface [42]. The charge-transfer resistance (R_{ct}) for composite KCP-800 (1.8 Ω) is much smaller than that of single-silk carbon KSW-800 (8 Ω), implying the synergistic action of two types of carbon materials. The R_{ct} decreases with the increasing of the activation temperature. The composite KCP-900 exhibits the smallest R_{ct} (0.37 Ω) and the lowest relaxation time (τ_0) of 3.1 s calculated by using the following equation [27]:

$$\tau_0 = \frac{1}{f_0}, \quad (1)$$

where f_0 is the frequency at phase angle of -45°. The KCP-800 electrode displays the smallest value of Z'' and the highest capacitance of 1.45 F (1000 mF·cm⁻²) at the low frequency of 10 MHz, calculated by the following equation [32]:

$$C = \frac{1}{2\pi f Z''}, \quad (2)$$

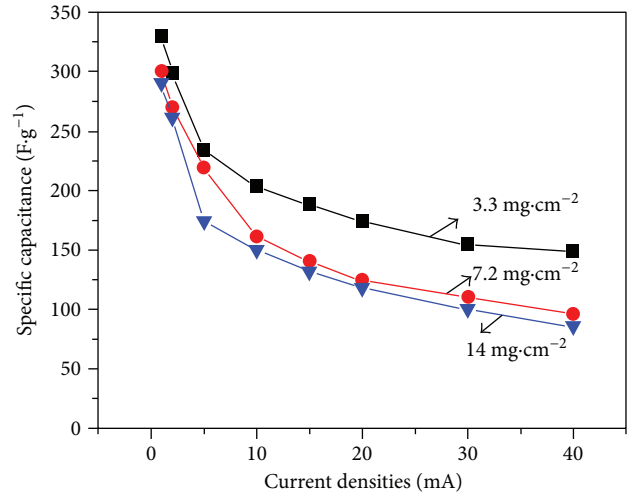


FIGURE 7: The dependence of the specific capacitance on the mass loading of active materials at different current densities.

where f is the frequency and Z'' is the corresponding imaginary impedance, which is in agreement with the CV and CP results.

The specific capacitances as a function of charge-discharge current densities for these electrodes measured by CP are shown in Figure 5(c). KCP-800 exhibits a maximum specific capacitance of 330 F·g⁻¹ at 0.5 A·g⁻¹, which is superior to the value of KCP-900 (242 F·g⁻¹), KCP-700 (218 F·g⁻¹), and single-silk carbon KSW-800 (288 F·g⁻¹). The specific capacitance is calculated from the following equation [29]:

$$C_s = \frac{I \times \Delta t}{m \times \Delta V}, \quad (3)$$

$$C_A = \frac{I \times \Delta t}{A \times \Delta V},$$

where C_s is the specific capacitance (F·g⁻¹), C_A is the area specific capacitance (F·cm⁻²), I is the applied working current (A), Δt is the discharge time (s), ΔV is the voltage range, m is the mass of the KCP of one electrode (g), and A is the total electrode area (cm²). It can be seen that the specific capacitance value of single-silk carbon KSW-800 (red line) decreases more significantly than that of the composite KCP (other lines), indicating the advantage of the combination of silk fibers and phenolic resin-derived carbon materials.

The electrochemical properties of KCP-800 were inspected from 10 to 100 mV·s⁻¹ using cyclic voltammetry (Figure 6(a)). The CV curves are close to rectangular shapes at scan rates from 10 to 100 mV·s⁻¹, indicating a good capacitive behavior of the electrode. It can be observed that KCP-800 possesses fast charge and discharge capability since a nearly linear dependence of current versus the scan rate is identified up to 100 mV·s⁻¹ (Figure 6(b)). Consistently, the charge/discharge curves in Figure 6(c) exhibit symmetric at different current densities, showing high reversibility and coulombic efficiency (ca. 92%). The KCP-800 electrode can

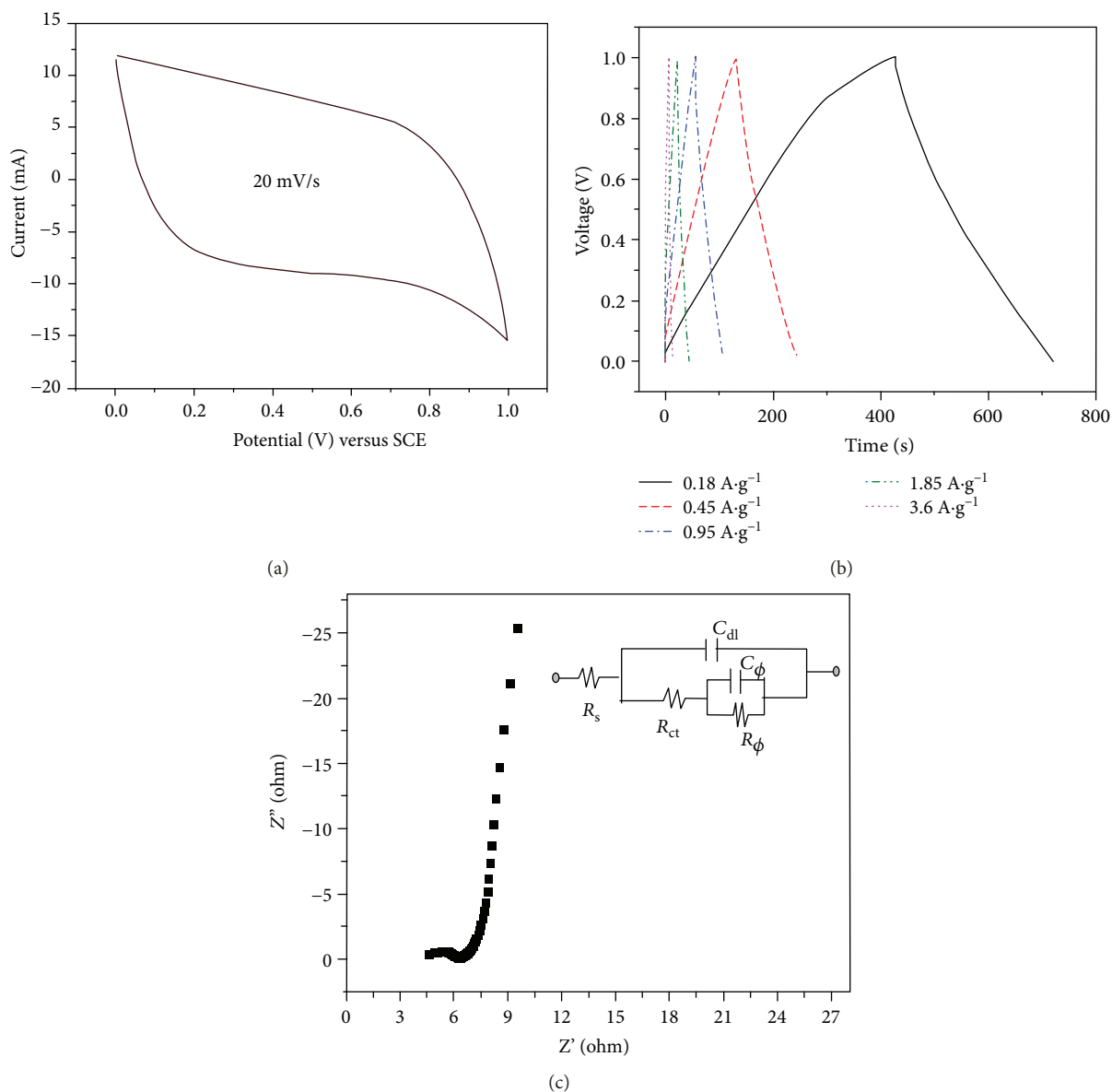


FIGURE 8: (a) CV curve of assembled symmetric ECs based on two KCP electrodes at a scan rate of 20 mV/s. (b) Galvanostatic charging/discharging curves of KCP//KCP symmetric ECs measured with different current densities. (c) Nyquist plots for KCP//KCP supercapacitor measured at 0 V DC potential; inset shows the corresponding equivalent circuit.

deliver an excellent specific capacitance of $330 \text{ F}\cdot\text{g}^{-1}$ at a current density of $0.5 \text{ A}\cdot\text{g}^{-1}$, which is higher than the values recently reported for carbon-based electrodes (Table 2). Even at the high current density of $12.5 \text{ A}\cdot\text{g}^{-1}$, KCP-800 can still achieve high charge storage values of $151 \text{ F}\cdot\text{g}^{-1}$, showing a high rate capability. The presence of hierarchical porosities and nitrogen/oxygen functionalities is responsible for the high capacitance and good rate capability. The cyclic stability of KCP-800 is also investigated by constant charge-discharge for 10000 cycles at current density of $3 \text{ A}\cdot\text{g}^{-1}$. As shown in Figure 6(d), it was retained about 91% of the initial capacitance, showing good stability of the electrode.

It is worth noting that the performance of the capacitors is closely related with thicknesses and mass loading of active materials [45, 46]. The thicker the electrode, the less efficient

is the ion diffusion. As a consequence, the great drop of the capacitive performance often occurs, especially at high loadings. Figure 7 shows the dependence of the specific capacitance on the mass loading of active materials at various charging/discharging current densities. As can be seen, the specific capacitance value at 1 mA decreases from $330 \text{ F}\cdot\text{g}^{-1}$ for $3.3 \text{ mg}\cdot\text{cm}^{-2}$ to $300 \text{ F}\cdot\text{g}^{-1}$ for $7.2 \text{ mg}\cdot\text{cm}^{-2}$ and $290 \text{ F}\cdot\text{g}^{-1}$ for $14 \text{ mg}\cdot\text{cm}^{-2}$, suggesting that the mass loading of KCP-800 impacts a little influence on the performance of the electrode. KCP-800 can still provide a significant specific capacitance for high mass loading even at high charge/discharge current density of 40 mA. These characters are attributed to the high surface area and excellent ionic diffusion within the hierarchical porous structures of the composite carbon electrode.

Two-electrode KCP//KCP symmetric ECs were also assembled and evaluated by CV, CP, and EIS techniques in 6 M KOH solution. Figure 8(a) shows the CV curve of two electrodes recorded over the voltage range of 1.0 V. The CV curve is close to rectangular shape at a scan rate of 20 mV/s, indicating a good capacitive behavior of the electrode. The galvanostatic charge-discharge profiles of the KCP//KCP ECs at different current densities are shown in Figure 8(b). The specific capacitance of the capacitor was calculated from the discharge curves with the values of 52.8, 51.0, 46.1, 37.8, and 22.3 F·g⁻¹ obtained from current densities of 0.18, 0.45, 0.9, 1.8, and 3.6 A·g⁻¹, respectively. The capacitance retained about 72% when the charge/discharge current density increased from 0.18 to 1.8 A·g⁻¹, suggesting the good rate capacity. The voltage drop at the initiation of the discharge is 0.07 V at the current density of 0.45 A·g⁻¹, implying a low electron series resistance (ESR) in the cell. The energy density E_s and power density of the symmetric capacitor are calculated by the following equation [11]:

$$\begin{aligned} E_s &= \frac{1}{2} C_s U^2, \\ P_s &= \frac{E_s}{t}, \end{aligned} \quad (4)$$

where C_s is the specific capacitance of the total mass of the two electrodes, U is the operating voltage of the cell, and t is the discharge time. The cell device achieved a maximum energy density of 7.4 Wh·kg⁻¹ at a power density of 90.1 W·kg⁻¹ and 5.3 Wh·kg⁻¹ at a power density of 900 W·kg⁻¹. Figure 8(c) shows the frequency response of the impedance for the KCP//KCP ECs. Nyquist plot displays a nearly linear and vertical characteristic at low frequency, indicating the capacitive behavior of the ECs. An equivalent circuit corresponding to the impedance responses achieved by ZSimpleWin software is in the inset of Figure 8(c), which exhibits the Faradaic pseudocapacitance (C_ϕ) in a parallel with the double-layer capacitance (C_{dl}), through the charge-transfer resistance (R_{ct}) and some possible further Faradaic discharge resistance (R_ϕ). The capacitance of the ECs arises from the combination of the Faradaic pseudocapacitance and the double-layer capacitance. The pseudocapacitance should be related to some participation of electrochemical surface reactions involving electron transfer of oxygen and nitrogen functionalities on the carbon electrode [40]. The KCP//KCP ECs show a low charge-transfer resistance (R_{ct}) of 1.9 Ω and a high capacitance of 0.63 F at the low frequency of 10 MHz calculated by the (2), suggesting that the KCP-800 electrode is a good candidate for ECs.

4. Conclusion

Hierarchical porous N- and O-doped carbon composites were successfully achieved by a combination of low molecular weight phenolic resin and silk fibers via a hydrothermal method followed by carbonization and KOH activation process. Due to the high surface area, enriched functional group, and hierarchical porous structures, the carbon composite showed excellent capacitive performance up to 330 F·g⁻¹

(or 1000 mF·cm⁻²) for 3.3 mg·cm⁻² loading and high rate capability. The prepared carbon shows a good storage capacitance even at high mass loading of active materials (290 F·g⁻¹ for 14 mg·cm⁻²). The combination of low molecular phenolic resin and silk fibers increases the surface area and enhances the electron transport within active materials. The KCP electrode symmetric ECs are able to deliver a maximum energy density of 7.4 Wh·kg⁻¹ in a voltage of 1.0 V with 6 M KOH electrolyte solution, suggesting a good prospect for practical applications.

Conflicts of Interest

The authors declare that they have no conflicts of interest.

Acknowledgments

The authors acknowledge the Liaoning Key Laboratory of Functional Textile Materials and Dalian Institute of Chemical Physics for the technical support of SEM, XRD, TEM, and BET measurements. The authors acknowledge the financial support by the National Natural Science Foundation of China (Project no. 51343002).

References

- [1] J. R. Miller, "Engineering electrochemical capacitor applications," *Journal of Power Sources*, vol. 326, pp. 726–735, 2016.
- [2] T. Brousse, D. Bélanger, and J. W. Long, "To be or not to be pseudocapacitive," *Journal of the Electrochemical Society*, vol. 162, no. 5, pp. A5185–A5189, 2015.
- [3] P. Simon and Y. Gogotsi, "Materials for electrochemical capacitors," *Nature Materials*, vol. 7, no. 11, pp. 845–854, 2008.
- [4] P. Simon, Y. Gogotsi, and B. Dunn, "Where do batteries end and supercapacitors begin?," *Science*, vol. 343, no. 6176, pp. 1210–1211, 2014.
- [5] A. Ghosh and Y. H. Lee, "Carbon-based electrochemical capacitors," *ChemSusChem*, vol. 5, no. 3, pp. 480–499, 2012.
- [6] A. González, E. Goikolea, J. A. Barrena, and R. Mysyk, "Review on supercapacitors: technologies and materials," *Renewable and Sustainable Energy Reviews*, vol. 58, pp. 1189–1206, 2016.
- [7] L. G. H. Staaf, P. Lundgren, and P. Enoksson, "Present and future supercapacitor carbon electrode materials for improved energy storage used in intelligent wireless sensor systems," *Nano Energy*, vol. 9, pp. 128–141, 2014.
- [8] A. Chen, Y. Yu, T. Xing, R. Wang, Y. Li, and Y. Li, "Synthesis of nitrogen-doped hierarchical porous carbon for supercapacitors," *Materials Letters*, vol. 157, pp. 30–33, 2015.
- [9] K. Fic, M. Meller, and E. Frackowiak, "Interfacial redox phenomena for enhanced aqueous supercapacitors," *Journal of the Electrochemical Society*, vol. 162, no. 5, pp. A5140–A5147, 2015.
- [10] A. K. Mondal, K. Kretschmer, Y. Zhao, H. Liu, H. Fan, and G. Wang, "Naturally nitrogen doped porous carbon derived from waste shrimp shells for high-performance lithium ion batteries and supercapacitors," *Microporous and Mesoporous Materials*, vol. 246, pp. 72–80, 2017.
- [11] W. Si, J. Zhou, S. Zhang, S. Li, W. Xing, and S. Zhuo, "Tunable N-doped or dual N, S-doped activated hydrothermal carbons derived from human hair and glucose for supercapacitor applications," *Electrochimica Acta*, vol. 107, pp. 397–405, 2013.

- [12] J. Wei, D. Zhou, Z. Sun, Y. Deng, Y. Xia, and D. Zhao, "A controllable synthesis of rich nitrogen-doped ordered mesoporous carbon for CO₂ capture and supercapacitors," *Advanced Functional Materials*, vol. 23, no. 18, pp. 2322–2328, 2013.
- [13] J. Jiang, L. Bao, Y. Qiang et al., "Sol-gel process-derived rich nitrogen-doped porous carbon through KOH activation for supercapacitors," *Electrochimica Acta*, vol. 158, pp. 229–236, 2015.
- [14] C. Zhang, R. Kong, X. Wang et al., "Porous carbons derived from hypercrosslinked porous polymers for gas adsorption and energy storage," *Carbon*, vol. 114, pp. 608–618, 2017.
- [15] J. Jiang, H. Chen, Z. Wang et al., "Nitrogen-doped hierarchical porous carbon microsphere through KOH activation for supercapacitors," *Journal of Colloid and Interface Science*, vol. 452, pp. 54–61, 2015.
- [16] P. Li, C. Xing, S. Qu, B. Li, and W. Shen, "Carbon dioxide capturing by nitrogen-doping microporous carbon," *ACS Sustainable Chemistry & Engineering*, vol. 3, no. 7, pp. 1434–1442, 2015.
- [17] Y. J. Kim, Y. Abe, T. Yanagiura et al., "Easy preparation of nitrogen-enriched carbon materials from peptides of silk fibroins and their use to produce a high volumetric energy density in supercapacitors," *Carbon*, vol. 45, no. 10, pp. 2116–2125, 2007.
- [18] Y. Zhu, S. Murali, M. D. Stoller et al., "Carbon-based supercapacitors produced by activation of graphene," *Science*, vol. 332, no. 6037, pp. 1537–1541, 2011.
- [19] J. Yi, Y. Qing, C. T. Wu et al., "Lignocellulose-derived porous phosphorus-doped carbon as advanced electrode for supercapacitors," *Journal of Power Sources*, vol. 351, pp. 130–137, 2017.
- [20] Q. Wang, J. Yan, Z. Dong, L. Qu, and Z. Fan, "Densely stacked bubble-pillared graphene blocks for high volumetric performance supercapacitors," *Energy Storage Materials*, vol. 1, pp. 42–50, 2015.
- [21] S. S. Balaji, A. Elavarasan, and M. Sathish, "High performance supercapacitor using N-doped graphene prepared via supercritical fluid processing with an oxime nitrogen source," *Electrochimica Acta*, vol. 200, pp. 37–45, 2016.
- [22] Y. Li, S. Zhang, H. Song, X. Chen, J. Zhou, and S. Hong, "New insight into the heteroatom-doped carbon as the electrode material for supercapacitors," *Electrochimica Acta*, vol. 180, pp. 879–886, 2015.
- [23] C. Tang, Y. Liu, D. Yang, M. Yang, and H. Li, "Oxygen and nitrogen co-doped porous carbons with finely-layered schistose structure for high-rate-performance supercapacitors," *Carbon*, vol. 122, pp. 538–546, 2017.
- [24] Q. Shi, R. Zhang, Y. Lv, Y. Deng, A. A. Elzatahrya, and D. Zhao, "Nitrogen-doped ordered mesoporous carbons based on cyanamide as the dopant for supercapacitor," *Carbon*, vol. 84, pp. 335–346, 2015.
- [25] Z. Gao, X. Liu, J. Chang et al., "Graphene incorporated, N doped activated carbon as catalytic electrode in redox active electrolyte mediated supercapacitor," *Journal of Power Sources*, vol. 337, pp. 25–35, 2017.
- [26] H.-F. Yen, Y. Y. Horng, M. S. Hu et al., "Vertically aligned epitaxial graphene nanowalls with dominated nitrogen doping for superior supercapacitors," *Carbon*, vol. 82, pp. 124–134, 2015.
- [27] T. Lin, I.-W. Chen, F. Liu et al., "Nitrogen-doped mesoporous carbon of extraordinary capacitance for electrochemical energy storage," *Science*, vol. 350, no. 6267, pp. 1508–1513, 2015.
- [28] K. Wang, M. Xu, Y. Gu, Z. Gu, and Q. H. Fan, "Symmetric supercapacitors using urea-modified lignin derived N-doped porous carbon as electrode materials in liquid and solid electrolytes," *Journal of Power Sources*, vol. 332, pp. 180–186, 2016.
- [29] Y. Chen, Z. Gao, B. Zhang, S. Zhao, and Y. Qin, "Graphene coated with controllable N-doped carbon layer by molecular layer deposition as electrode materials for supercapacitors," *Journal of Power Sources*, vol. 315, pp. 254–260, 2016.
- [30] L. Qie, W. Chen, H. Xu et al., "Synthesis of functionalized 3D hierarchical porous carbon for high-performance supercapacitors," *Energy & Environmental Science*, vol. 6, no. 8, pp. 2497–2505, 2013.
- [31] J. Shao, F. Ma, G. Wu et al., "Facile preparation of 3D nanostructured O/N co-doped porous carbon constructed by interconnected carbon nanosheets for excellent-performance supercapacitors," *Electrochimica Acta*, vol. 222, no. 20, pp. 793–805, 2016.
- [32] B.-X. Zou, Y. Gao, B. Liu, Y. Yu, and Y. Lu, "Three dimensional heteroatom-doped carbon composite film for flexible solid-state supercapacitors," *RSC Advances*, vol. 6, no. 6, pp. 4483–4489, 2016.
- [33] X. He, H. Yu, L. Fan, M. Yu, and M. Zheng, "Honeycomb-like porous carbons synthesized by a soft template strategy for supercapacitors," *Materials Letters*, vol. 195, pp. 31–33, 2017.
- [34] K. S. W. Sing, "Reporting physisorption data for gas/solid systems with special reference to the determination of surface area and porosity (provisional)," *Pure and Applied Chemistry*, vol. 54, no. 11, pp. 2201–2218, 1982.
- [35] X. Xu, J. Gao, Q. Tian, X. Zhai, and Y. Liu, "Walnut shell derived porous carbon for a symmetric all-solid-state supercapacitor," *Applied Surface Science*, vol. 411, pp. 170–176, 2017.
- [36] H. Jin, X. Wang, Z. Gu, Q. Fan, and B. Luo, "A facile method for preparing nitrogen-doped graphene and its application in supercapacitors," *Journal of Power Sources*, vol. 273, pp. 1156–1162, 2015.
- [37] D. Liu, C. Zeng, D. Qu et al., "Highly efficient synthesis of ordered nitrogen-doped mesoporous carbons with tunable properties and its application in high performance supercapacitors," *Journal of Power Sources*, vol. 321, pp. 143–154, 2016.
- [38] X. Laloyaux, E. Fautré, T. Blin et al., "Temperature-responsive polymer brushes switching from bactericidal to cell-repellent," *Advanced Materials*, vol. 22, no. 44, pp. 5024–5028, 2010.
- [39] F. Gao, J. Qu, Z. Zhao, Z. Wang, and J. Qiu, "Nitrogen-doped activated carbon derived from prawn shells for high-performance supercapacitors," *Electrochimica Acta*, vol. 190, pp. 1134–1141, 2016.
- [40] D.-W. Wang, F. Li, L.-C. Yin et al., "Nitrogen-doped carbon monolith for alkaline supercapacitors and understanding nitrogen-induced redox transitions," *Chemistry - A European Journal*, vol. 18, no. 17, pp. 5345–5351, 2012.
- [41] B. You, L. Wang, L. Yao, and J. Yang, "Three dimensional N-doped graphene-CNT networks for supercapacitor," *Chemical Communications*, vol. 49, no. 44, pp. 5016–5018, 2013.
- [42] B.-X. Zou, Y. Liang, X. X. Liu, D. Diamond, and K. T. Lau, "Electrodeposition and pseudocapacitive properties of tungsten oxide/polyaniline composite," *Journal of Power Sources*, vol. 196, no. 10, pp. 4842–4848, 2011.
- [43] Z. Bo, S. Mao, Z. Jun Han, K. Cen, J. Chen, and K. (. K.). Ostrikov, "Emerging energy and environmental applications

- of vertically-oriented graphenes,” *Chemical Society Reviews*, vol. 44, no. 8, pp. 2108–2121, 2015.
- [44] X. He, H. Ma, J. Wang, Y. Xie, N. Xiao, and J. Qiu, “Porous carbon nanosheets from coal tar for high-performance supercapacitors,” *Journal of Power Sources*, vol. 357, pp. 41–46, 2017.
- [45] Y. Gogotsi and P. Simon, “True performance metrics in electrochemical energy storage,” *Science*, vol. 334, no. 6058, pp. 917–918, 2011.
- [46] K. Shi and I. Zhitomirsky, “Fabrication of polypyrrole-coated carbon nanotubes using oxidant–surfactant nanocrystals for supercapacitor electrodes with high mass loading and enhanced performance,” *ACS Applied Materials & Interfaces*, vol. 5, no. 24, pp. 13161–13170, 2013.



Hindawi
Submit your manuscripts at
www.hindawi.com

